Optoplasmonic detection of single particles and molecules in motion

Asgari, N.

3

Nanosecond time scale transient optoplasmonic detection of single proteins

Optical detection of individual proteins with high bandwidth holds great promise for understanding important biological processes on the nanoscale and for high-throughput fingerprinting applications. As fluorescent labels impose restrictions on detection bandwidth and require time-intensive and invasive processes, label-free optical techniques are highly desirable. Here, we read out changes in the resonantly scattered field of individual gold nanorods interferometrically and use photothermal spectroscopy to optimize the experiment's parameters. This interferometric plasmonic scattering enables the observation of single proteins as they traverse plasmonic near fields of gold nanorods with unprecedented temporal resolution in the nanosecond-to-microsecond range.

[1]Baaske, M. D., Asgari, N., Punj, D., & Orrit, M. (2022). Nanosecond time scale transient optoplasmonic detection of single proteins. Science Advances, 8(2), eabl5576.

3.1 Introduction

Almost all biological processes involve enzymatic action. Enzyme function is often accompanied by conformational changes that can occur on microsecond time scales-substantially faster than the enzyme's turnover rate [80]. Essential elementary steps in protein folding and unfolding may occur on microsecond [81, 82] and even nanosecond [83] time scales. As probing assays for such fast dynamics often rely on single-molecule fluorescence, they require the analysis of thousands of single molecules [30]. The need for such massive numbers arises directly from the limited bandwidth of fluorescence detection and from the restrictions in observation time imposed by dye blinking and bleaching. The biological processes discussed above have one thing in common: They involve motion. Therefore, label-free methods with high bandwidth able to resolve such motion are highly desirable. Here, we propose observations of the diffusive motion of whole proteins as a starting point for the development of such methods. In addition, the observation of protein motion by itself holds great promise for high-throughput fingerprinting applications. Translational and rotational motion carries information about such protein properties as size and shape. Protein charge and dipole moment can be probed by electrophoresis and dielectrophoresis if the sample is subjected to external electric fields. Optoplasmonic methods are promising candidates as high-bandwidth sensing platforms, as single-molecule sensitivity has been demonstrated repeatedly [28, 31, 33, 34, 71]. State-of-the-art optoplasmonic methods typically exhibit time resolutions on the order of milliseconds and rely on analyte immobilization to facilitate detection. The need for analyte immobilization is a direct consequence of the minuscule dimensions of plasmonic near fields typically providing sub-attoliter–sized detection volumes that, in turn, demand sub-microsecond temporal resolution for the direct detection of proteins in motion. Here, we show that such temporal resolution can indeed be achieved. We demonstrate the observation of single proteins as small as hemoglobin (Hem, molecular weight (MW):64 kDa) as they traverse plasmonic near fields of gold nanorods (GNRs) and interact with their surface, all while maintaining signal-to-noise ratios (SNRs) larger than 5 and an unprecedented temporal resolution well below microseconds. This method enables the label-free observation of single-molecule dynamics on previously inaccessible time scales.

3.2 Result

3.2.1 Sensor principle

To achieve such resolution, we have improved the confocal system we had previously used to detect single metal nanoparticles in Brownian motion [18]. Our system recognizes perturbations of dielectric environment inside a plasmonic GNR's near field caused by nano-objects such as nanoparticles, micelles, or proteins. Such perturbations alter the GNR's polarizability and shift the frequency ν_{NR} of its localized surface plasmon resonance (LSPR), resulting in a change of the scattered field's amplitude Es and its phase difference ϕ with respect to the incident field. The quantity we detect is the intensity $I_{det} \propto |E_r|^2 + |E_s|^2 + 2|E_r|\ |E_s|\ cos(\phi + \gamma)$, which is a result of the interference between scattered E_s and reflected E_r fields with phase difference $\phi + \gamma$, where γ denotes the Gouy phase. More specifically, we are interested in its changes

$$\Delta I_{det} \propto \Big[|E_s| + |E_r|cos(\phi + \gamma)\Big]\Delta|E_s| - |E_r||E_s|\ sin(\phi + \gamma)\ \Delta\phi, \tag{3.1}$$

Here, the left-hand $\Delta|E_s|$ term, which denotes the change of the scattered field, is the quantity typically detected by interference scattering methods [84, 85]. which aim to recognize the transition between the absence and the presence of a, not necessarily resonantly, scattering nano-object. In contrast, our method aims to detect changes in the cross section and resonance frequency of an otherwise static resonant scatterer. In this case, the $\Delta\phi$ term gains importance for field-strength ratios $R_F = |E_s/E_r| < 1$. Established interference scattering based methods use selective reduction of the reflected beam's intensity by spatial filtering [86, 87] to tune R_F and optimize contrast. We, however, can make use of the GNR's scattering anisotropy and tune R_F via choice of incident and analyzed linear polarizations [84]. Disregarding GNR dimensions and fixing the GNR's position in the center of the probe beam, we have access to four adjustable parameters that influence the sensitivity of a single NR: Incident and analyzed polarizations tune R_F, the probe laser's frequency tunes R_F and ϕ, and the Gouy-phase γ can be adjusted via the distance Δz between GNR and the objective's focal plane. Other parameters that affect SNRs are probe power, NR dimensions, LSPR linewidth, and hardware specifications like the noise-equivalent power (NEP) and excess noise factor of the detector. The optimization of parameters based on the observation of signal amplitudes resulting from random perturbations caused by diffusing analytes [18] is too slow and too indirect. We are thus looking for a means that enables us to directly probe our system's response to changes in an GNR's po-

larizability that (i) is independent of analyte properties, (ii) does not involve chemical modification of the GNR, and (iii) can be easily controlled and implemented. We found that photothermal spectroscopy is a convenient method that fulfills all of these requirements.

3.2.2 Photothermal calibration

Photothermal spectroscopy detects minute changes in refractive index that follow the absorption of light by an analyte and the consequent dissipation of heat into the surrounding medium [61, 64]. Here, we use the sensor NR as absorber. Absorption of the intensity-modulated heating beam (wavelength: 532 nm) alters the polarizability of the GNR via the thermo-refractive effect and gives rise to changes in the probe beam's intensity at the heating beam's modulation frequency ν_H. This process is similar to analyte-induced changes of GNR polarizability and is a result of the same contrast mechanism, namely, the change of effective dielectric contrast between the GNR and the surrounding medium. In consequence, the photothermal response is well suited as a proportional probe for relative changes in detected intensity $\Delta I_{Det}/I_{Det}$. Specifically, we determine the relative photothermal amplitude $A_{PT} = \frac{A(\nu_H)}{A(\nu_P)}$, where $A(\nu)$ denotes the root mean square (rms) amplitude at the respective modulation frequency ν. Here, ν_P is the intensity modulation frequency of the probe beam (wavelength range: 785 ± 20 nm). We use double modulation at ν_H=1.3 MHz and ν_P=1 MHz to reject contributions from $1/f$-noise. Our setup (see figure. 3.1A) enables us to obtain white-light scattering spectra and thus to select GNRs with sufficient overlap between LSPR and our probe laser's tuning range. Rotation of polarizer and analyzer orientations in parallel configuration further allows us to determine GNR orientation. In the following, we restrict the parameter space by aligning the orientations of incident and analyzed polarization parallel to the GNR's long axis and centering of the GNR's position in the probe beam's focus. For our measurements, we use GNRs with dimensions of 25×80 nm^2 and 40×110 nm^2 and typical LSPRs of 1.6 eV (774 nm). For GNRs with ≈40 nm diameter, $R_F \gg 1$, and the interference terms in equation. 3.1 are negligibly small. In this case, high A_{PT} values are found for probe wavelengths coinciding with the flanks of the NR's LSPR spectrum, *i.e.*, where the slopes of the Lorentzian are highest (see figure. 3.1B, left). For the 25- to 20-nm-diameter GNRs, $R_F \approx 1$ and high A_{PT} values are found closer to the LSPR's center (see figure. 3.1B, center and right). This is expected as $\phi(\nu_P)$ has the highest slopes in proximity to the LSPR frequency and indicates that for GNRs with smaller diameters, the $\Delta\phi$ term in

equation. 3.1 becomes increasingly dominant.

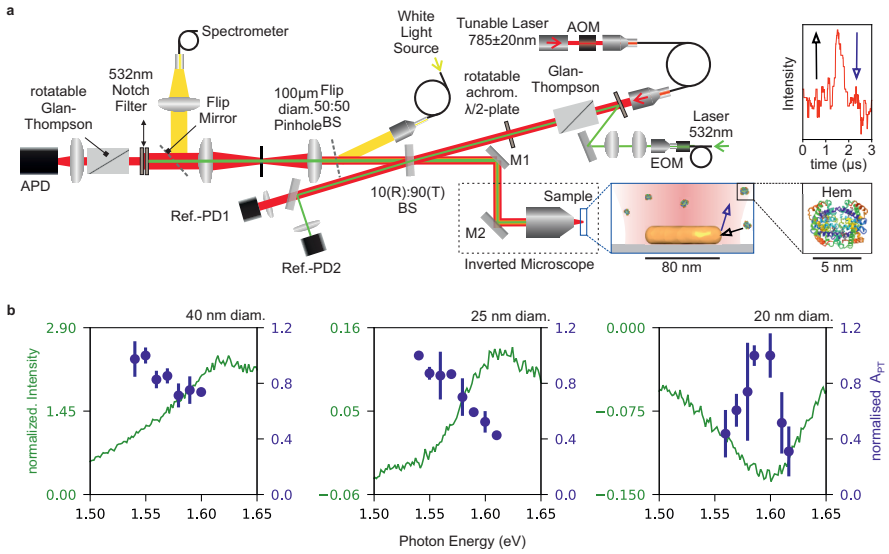

Figure 3.1: Experimental setup with photothermal signal optimization. a) The optical setup (left) alongside an illustration of a Hem molecule entering and perturbing an GNR's near field (bottom center) and an example of a measured intensity trace showing a short burst caused by such perturbation (top right). Arrows indicate entry and exit of a Hem molecule into and out of the GNR's near field and respective changes in detected intensity. **b)** Sections of white-light scattering spectra normalized to the reflection on the glass slide (green line) and the corresponding relative photothermal amplitude A_{PT} values (blue dots) obtained while varying the tunable laser's wavelength for GNRs with various diameters.

Moreover, adjustment of γ via detuning of Δz away from 0 allows us to offset the maxima of the interference terms with respect to ν_{NR} and gives rise to asymmetric spectra (see figure. 3.1B, center). To streamline the alignment process, we follow a simple recipe for all GNRs: We first center the NR in the focus (xyz) by maximizing the scattered intensity with crossed polarizers. Then, we optimize A_{PT} with parallel polarizers aligned along the GNR's long axis by first tuning the probe wavelength and then adjusting the GNR position along the focal axis (z).

3.2.3 Single-molecule measurements

Single-molecule measurements are typically performed by recording intensity time traces of 10 ms length with a sampling rate of 100 MHz using analog avalanche photodiodes working in the linear regime with -3-dB cutoff frequencies of 400 MHz (APD1)

and 200 MHz (APD2) whereas in the case of APD1, a low-pass filter with a -3-dB cutoff frequency of 190 MHz was inserted between detector and oscilloscope. These traces are then denoised by applying a running 10-point median filter. Specifically, we detect glucose oxidase (GOx; MW≈ 160 kDa) from bovine blood (figure. 3.2B) [88] molecules as they move through the GNR's near field.

These molecules produce transient shifts of the LSPR, which are recognized as changes of the detected intensity (see equation. 3.1). These changes appear on the intensity traces as patterns of two different types: (i) short spike-like perturbations (compare figure. 3.2A, I-1, II-1 left, and III-2, and figure. 2B, II-1, II-2, and III-2), which we interpret as protein molecules moving directly in and out of the near field; and (ii) level-transition patterns (compare figure. 3.2A, I-1 and III-1 center, and figure. 3.2B, I, III-1, and IV-1), which we attribute to protein molecules moving through the aqueous medium into the near field and then dwelling at the GNR's surface owing to attractive forces until the attractive potential is eventually overcome and they again move out of the near field. We also observed a few binding and unbinding events without their respective counterparts in the same trace. This means that sticking lasting longer than the trace length of 10 ms can occur. To obtain statistics, we count fluctuations on intensity traces as events if their amplitudes exceed 5σ, where σ is the SD of the whole trace. This does not include rare single-step events without counterpart in the same trace (GOx). GOx measurements were performed using the DC-coupled APD1. For the Hem measurements APD2 was used. APD2 is AC-coupled and, because of its low-frequency cutoff (1.5 kHz) can introduce artificially decaying amplitudes on longer events. To avoid contributions from these artifacts, events with durations longer than 0.1 ms were excluded from analysis. For each event, we determine the maximum amplitudes δI_{max} and the following temporal properties: $\tau_{rise}(\tau_{fall})$, the rise (fall) time, *i.e.*, the time it takes from the beginning (end) of the event to rise (fall) to (from) half the maximum, and the duration between these points, *i.e.*, the full duration at half maximum (FDHM). For both Hem and GOx, we find rise and fall times in the range from 10 to 1000 ns (see figure. 3.3 left A,B). All τ_{rise} and τ_{fall} distributions fit well to mono-exponential decays [*i.e.*, to $f(t) = N\frac{t}{\tau}e^{-t/\tau}$] for the logarithmically spaced distributions] and we find rise (fall) decay times of 101±8 ns (108±6 ns) for GOx and 153±11 ns (155±11 ns) for Hem. The similarity between rise- and fall-time distributions suggests that entry and the exit processes of both proteins into and out of the GNR's sensitive volume are subject to equivalent interactions.

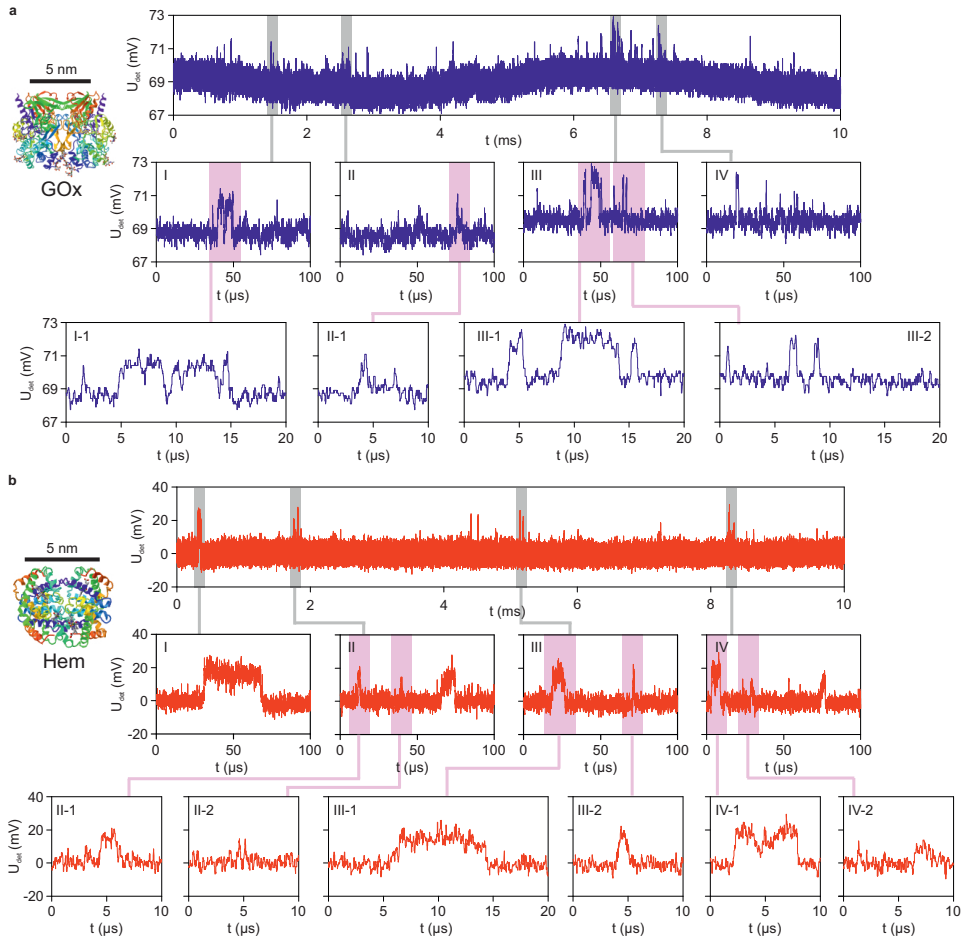

Figure 3.2: Transient single-protein detection. Intensity perturbations due to GOx (blue) and Hem (red) molecules moving in an GNR's near field. **A)** Trace (top) and shorter time scale subtraces (I to IV) showing perturbations caused by GOx molecules observed with a 25-nm-diameter NR and a DC-coupled detector. **B)** Trace (top) and shorter time scale subtraces (I to IV) showing perturbations caused by Hem molecules observed with a 40-nm-diameter NR and an AC-coupled detector. Most perturbations exhibit sub-microsecond rise and fall times. Longer perturbations as shown in (A), I-1 and III-1 center, and (B), I, III-1, and IV-1, are likely caused by attractive interactions between analyte and GNR. All traces were recorded with Δt =10 ns and denoised with a 10-point median filter. Protein concentrations were 500 nM (A, GOx) and 30 nM (B, Hem).

The two-dimensional (2D) histograms (figure. 3.3, A and B, left) further exhibit no apparent correlation between τ_{rise} and τ_{fall} for individual events. This missing correlation shows that entry and exit processes into and out of near field are mutually

independent as expected for Brownian motion. The rise and fall times for GOx are shorter than the ones we find for Hem although GOx exhibits the higher molecular weight. We attribute this difference to two factors: (i) The difference between the near-field extents due to the different dimensions of the GNRs used for these measurements. GOx was observed with the smaller GNR and thus we expect shorter rise and fall times. (ii) Contributions due to rotational diffusion of the more anisotropic GOx (in comparison to the globular Hem). We find distinctive differences between the intensity autocorrelation curves of both molecules. Specifically, we observe a continued increase in correlation toward shorter times on the sub-100-ns scale for GOx, which is absent for Hem. This time scale agrees well with the estimated rotational diffusion time of GOx, on the order of 50 ns, and lies within our temporal resolution. Rotational and translation diffusion are coupled and, for our system, exhibit similar characteristic times in the 10- to 100-ns range. Thus, a clear distinction between contributions by both processes on a single-event basis is challenging and further work beyond the scope of this manuscript is needed to confirm the observation of rotational diffusion. We now want to discuss the FDHM distributions found for both protein species. These times represent the dwell time of individual proteins in the NR's sensitive volume. They are centered around $\approx$1 µs and distributed over ranges from 100 ns up to few tens of microseconds, *i.e.*, substantially longer than the rise and fall times alone (see figure. 3.3b left). Here, the stretch toward long time scales is likely due to attractive interactions between the proteins and the GNR's surface and indicates unspecific sticking. The FDHM distribution of Hem (figure. 3.3b right) is more stretched toward long times than the one of GOx (figure. 3.3a right). Specifically, we find that the FDHM distribution for GOx fits well to a mono-exponential decay as expected for a Langmuir adsorption process governed by a single time constant for which we find τ=0.9 µs from the respective fit. For Hem, this is not the case, as the single-rate fit clearly deviates from the data (not shown). This suggests contributions from multiple processes with different rates. Already for two rates (τ_1=0.83 µs and τ_2=4.8 µs), we find a much better match. This is rather expected because of the larger set of fitting parameters. We, however, think that a broader spectrum of rates exists rather than just two. The maximum amplitude versus FDHM istribution for Hem (figure. 3.3b right) also reveals a stronger correlation between larger amplitudes and longer times as compared with GOx (figure. 3.3a right).

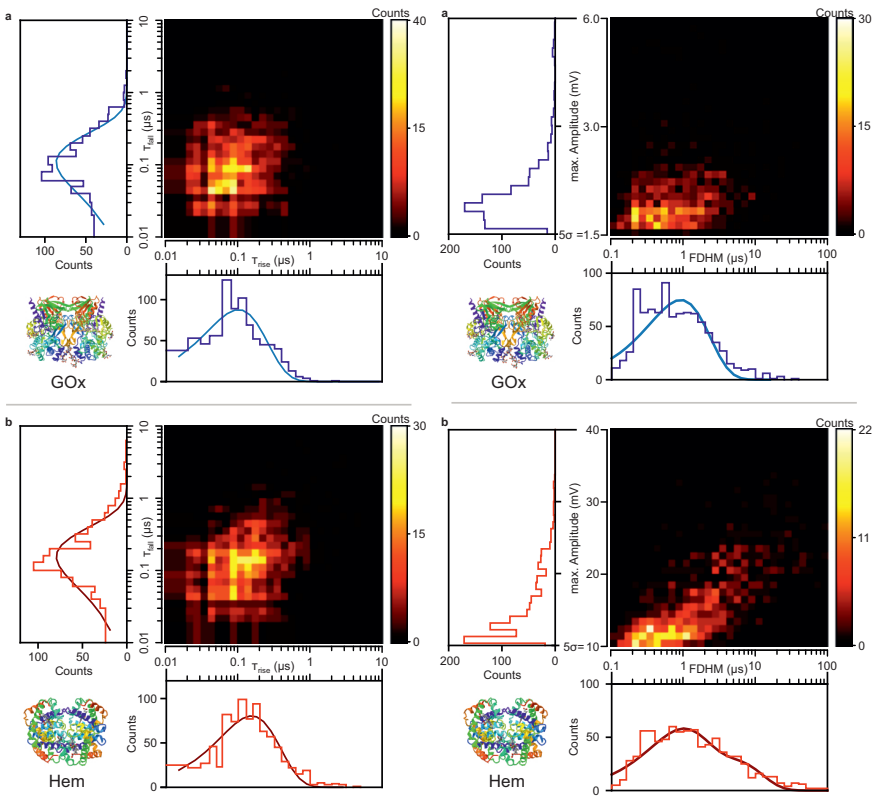

Figure 3.3: a,b left) Rise and fall time distributions of single-protein detection events. Statistics of rise and fall times, characterizing the molecular diffusion in the absence of sticking and immediately before and after sticking, for GOx (A) and Hem (B). Each panel (A and B) shows the τ_{rise} (bottom) and τ_{fall} (right) distributions alongside their respective two- dimensional (2D) histograms (center). Solid lines (A, light blue and B, dark red) in the distributions show fits to mono-exponential time distributions plotted on logarithmic scale of times. **a,b right) Dwell time and amplitude distributions of single-protein detection events.** Statistics of dwell times and amplitudes as obtained for GOx (A) and Hem (B). Each panel (A and B) shows the full duration at half maximum (FDHM) (bottom) and maximum amplitude (right) distributions alongside their respective 2D histograms (center). Solid lines in the FDHM distributions show fits to mono-exponential (A, light blue) and bi-exponential time distributions, plotted on logarithmic scale of times (B, dark red).

We think that the differences between Hem and GOx, specifically the existence of multiple rate constants is due to one of the following reasons: (i) Hem exhibits surface areas that have different affinity to gold and therefore Hem shows different sticking dynamics dependent on the protein's contact area with the surface. In this case, the correlation of high amplitudes with long FDHMs arises because of increased

overlap between protein sections with high polarizability (*i.e.*, Hem's iron complex) and the GNR's near field. (ii) Hem has different affinities to different types of gold crystal facets. In this case, the correlation of higher maximum amplitudes with longer FDHMs implies that facets that offer higher affinities coincide with zones of higher near-field intensity. Which hypothesis is right or whether there is a process we have not covered will require further study beyond the scope of this work.

3.2.4 Proof of single-protein detection

In the following, we will provide evidence based on multiple aspects of our data and complementary measurements, which, together, provide strong evidence that the observed events indeed arise form perturbation caused by single-protein molecules.

1) Time scales of event dynamics: For both GOx and Hem, we observed rise and fall times on the order of 105 and 155 ns respectively. To evaluate the distance dependence of the observed amplitudes, we have performed boundary element method (BEM) [89] simulations of our GNR-protein systems. From those simulations, we find decay lengths of $d_{L,Hem}$ =8.4 nm for the respective systems. Using these values as rms displacements and the rise and fall times as diffusion time, we can determine the hydrodynamic radius of our analytes via the Stokes-Einstein relation:

$$r_H = \frac{k_B T\ \tau_{fall}}{\pi\eta\ d_{half}^2}, \tag{3.2}$$

where k_B is Boltzmann's constant, T is the temperature, and η is the viscosity of water. We find $r_H = 2.8\pm0.6$ nm for Hem, which is an excellent match with the literature value of 3.11 nm [90, 91] and agrees well with the value of 3.9 ± 1.1 nm determined via dynamic light scattering. For GOx, we find $r_H = 5.8\pm 1.3$ nm, a value that within the error comes close to the literature values of 4.45 nm [92] and 5.7 nm [93] and agrees well with the value of 5.3 ± 1.3 nm determined via DLS.

2) Amplitude of detected events: Here, we first have to point out that GOx and Hem measurements performed with different detectors; *i.e.*, the amplitude values given are not directly comparable. To obtain a direct comparison of perturbation amplitudes, we determine the relative intensity changes $\Delta I_{rel} = |\frac{\Delta I_{max}}{\overline{I_{det}}}|$ caused by GOx and Hem from measurements performed with the same DC- coupled detector and GNRs of similar dimensions. We find average values of $\Delta\overline{I_{det}} = (3.4 \pm 1.5)\%$ for GOx and $(1.55 \pm 0.45)\%$ for Hem. From BEM simulations of our GNR-protein systems, we find maximum relative changes in the scattering cross sections with values of $\Delta\sigma_{Hem} = 0.8\%$ and $\Delta\sigma_{GOx} = 1.74\%$. These values are a factor ≈ 2 lower than the experimental

values. This discrepancy is a direct result of our measurement methodology, *i.e.*, the use of interference scattering. For the GNRs used here, we experimentally determined values of $R_F^2 = 1.7$ (Hem) and $R_F^2 = 1.8$ (GOx). From these values and our BEM simulation results, we determine upper bounds for the ΔI_{rel} values achievable via our interference-based method. We find $\Delta I_{rel,max} = 1.9\%$ for Hem and $\Delta I_{rel,max} = 3.5\%$ for GOx. These values are 2.4- and 2-fold higher than the ones achievable by pure scattering-based methods and agree well with our experimental results. Moreover, also the ratio $\Delta I_{GOx}/\Delta I_{Hem} = 1.84$ is in good agreement with the experimental value of $\Delta\overline{I_{rel}}(GOx)/\Delta\overline{I_{rel}}(Hem) = 2.2 \pm 1$. In the case of GOx, some of the experimental ΔI_{rel} values exceed the upper bound. We attribute this discrepancy to the fact that we simulated both proteins as spheres. We believe that this simple model results in an underestimation of the intensity changes caused by GOx, which deviates more from a spherical shape than Hem. Zijlstra *et al.* [28] had observed a similar discrepancy between simulations on the basis of spherical models and their experimental results, which yielded LSPR shifts ≈ 2 times higher than expected.

3) Statistical evidence: We have performed measurements at different analyte concentrations and find a linear dependence between event rate and analyte concentration. We also find that the inter-event times follow a Poissonian distribution. Both findings together prove that events are mutually independent and are caused neither by multiple simultaneous entry of multiple proteins into the near field nor by the formation of aggregates, processes for which a nonlinear scaling between rate and concentration is expected. In addition, we did not detect events in the absence of analytes. Thus, the presence of impurities with non- negligible concentrations in the used supernatants can be ruled out. Together, these three arguments provide convincing evidence that we indeed detect single proteins.

3.3 Conclusion

We think that being able to resolve and analyze such short unspecific interactions opens up a whole new pathway for fast molecular fingerprinting. We envision that previously hidden differences in the interaction dynamics between specific protein subdomains and small weakly bonding receptor molecules on the GNR's surface may be used as means to distinguish between proteins of similar mass. In the simplest case, the average number of formed bonds determines the dwell time. This would further allow us to gain structural information on analytes, especially unknown ones, therefore mitigating the need for target-specific receptors. In addition, physical analyte properties such as

Stokes radius and molecular weight may be determined via τ_{rise}, τ_{fall}, and relative amplitudes following GNR calibration with a suited standard. We further envision that in combination with purpose-tailored plasmonic structures, which will improve on the relatively modest enhancement and confinement of GNR near fields, our method will be able to resolve fast changes in the structure and shape of single proteins purposely positioned inside their near fields.

In conclusion, we have demonstrated the transient detection of single proteins with masses as low as 64 kDa traversing the sub-attoliter volumes spanned by plasmonic near fields during times as short as 100 ns and with an SNR exceeding 5. We have used our unprecedented temporal resolution to observe protein motion. From our experiments, we determined hydrodynamic radii that agree well with literature values and with complementary DLS measurements. Moreover, relative signal amplitudes scale as expected and agree with simulation results. We further found initial evidence that suggests that our method may resolve rotational diffusion and thus provide information on protein anisotropy. This shows that our method can simultaneously probe Stokes radius and polarizability of a protein and demonstrates its potential for future high-throughput fingerprinting applications. By observing the dynamics of unspecific protein-surface interactions, we also found distinctive differences in sticking behaviors of GOx and Hem. We think that this result offers but a glimpse of the additional information that may be gained on physical and biochemical processes, now made accessible by fast optoplasmonic detection.

3.4 Supplementary information

3.4.1 Autocorrelation measurements

Here we show intensity autocorrelations of the light scattered by the nanorod, for Hemoglobin and Glucose Oxidase. Autocorrelations were computed directly from intensity traces with 10 ms durations and dt =10 ns following the procedures used in our previous work. Results are averaged over 50 consecutively recorded traces and shown in figure. 3.4. For Glucose Oxidase we find strong correlations on timescales shorter than 100 ns, whereas no such correlations are present for Hemoglobin. Glucose Oxidase presents the shape of two cylinders co-joined orthogonal to the cylinder axis and therefore possess a higher asymmetry then the globular Hemoglobin. Therefore we think it is likely that the difference between the autocorrelation is due to rotational diffusion. This hypothesis is further supported as we find good agreement between

the observed correlation times <100 ns and the rotational diffusion times τ_D of 28 to 129 ns expected for a sphere with the dimensions of Glucose oxidase, *i.e.* radii of 3 to 5 nm. Calculations were performed using the relation $\tau_D = (6D)^{-1}$ whereas the rotational diffusion constant D was determined via the Debye-Stokes-Einstein relation: $D = \frac{k_b T}{8\pi\eta r_h^3}$, where k_B is Boltzmann's constant, T the temperature (here 293 K), η denotes the dynamic viscosity of the medium (here water $\eta = 10^{-3}$ Pa) and r_h is the diffusor's hydrodynamic radius.

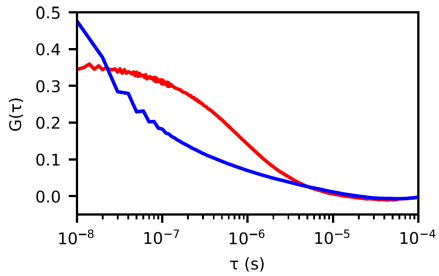

Figure 3.4: Protein autocorrelation curves. Averaged intensity autocorrelations measured for Glucose Oxidase (blue, GNR dimensions: 52×15 nm^2). Only the autocorrelation curve of the more asymmetric Glucose Oxidase exhibits an additional increase on timescales shorter than 100 ns. This increase coincides with the expected rotational diffusion times of 28 to 129 ns.

3.4.2 SEM-Micrographs and Sizes of Gold Nanorods

Here we show the dimensions of the gold nanorod samples used in this manuscript (see figure. 3.5). We further compare NR diameters as determined via SEM and optical means, *i.e.*, via normalized white-light scattering spectra and polarisation angle rotation (see figure. 3.6).

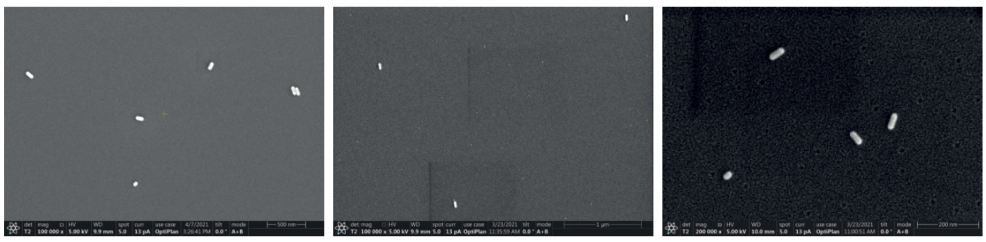

Figure 3.5: Example SEM micrographs of nanorod samples. NRs exhibit average diameters of 40, 25, and 20 nm (left to right). GNRs have various aspect ratios and suited candidates are selected based on their white-light spectra.

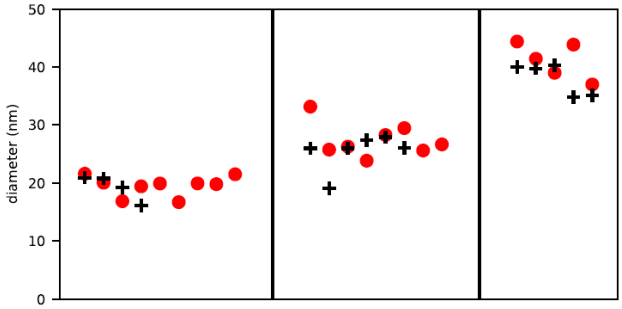

Figure 3.6: Comparison of nanorod diameters determined via optical means and SEM. Diameters determined via optical measurements are shown as black crosses and diameters determined from SEM micrographs are depicted as red circles. Samples are not correlated, *i.e.*, different GNRs are observed via both methods. We used three different commercial GNR samples, which are separated by the vertical lines.

3.4.3 BEM Simulations

We perform boundary element method (BEM) simulations using MNPBEM [89] specifically we simulate 3 systems illustrated in figure. 3.7a.

- System I consists of a gold NR with a diameter of 40 nm and a length of 110 nm together with a Hemoglobin (Hem) Molecule modeled as a 6.22 nm diameter sphere of refractive index (RI) 1.5 immersed in water with an RI of 1.33.
- System II consists of a gold GNR with a diameter of 25 nm and a length of 80 nm together with a Hemoglobin (Hem) Molecule modeled as a 6.22 nm diameter sphere of RI 1.5 immersed in water with an RI of 1.33.
- System III consists of a gold GNR with a diameter of 25 nm and a length of 80 nm together with a Glucose Oxidase molecule modeled as a 8.9 nm diameter sphere of RI 1.5 immersed in water with an RI of 1.33.

In all three cases the protein-spheres were placed on the nanorod's long axis at a distance d from its tip. We first simulated scattering spectra for all 3 systems $\sigma_k(\lambda)$, where i indicates the system number and then determined the relative changes of scattering cross sections

$$\Delta\sigma_k(\lambda) = \left|(\sigma_k(\lambda) - \sigma_0(\lambda))/\sigma_0(\lambda)\right|, \tag{3.3}$$

where σ_0 denotes the scattering spectra of the GNR used in system k, immersed in water of RI 1.33 and without the protein. In all cases the protein spheres were placed

at a distance of d =0.1 nm from the tips and the polarization of the incident plane wave was aligned with the GNR's long axis. The corresponding results are shown in figure. 3.7b. From these changes in relative intensity $\Delta\sigma_k(\lambda)$ we then determined the wavelength $\lambda_{k,max}$ to 778.188 nm for system I and 773.145 nm for System II and III and consequently computed $\Delta\sigma_k$ values for different distances (see figure. 3.7c).

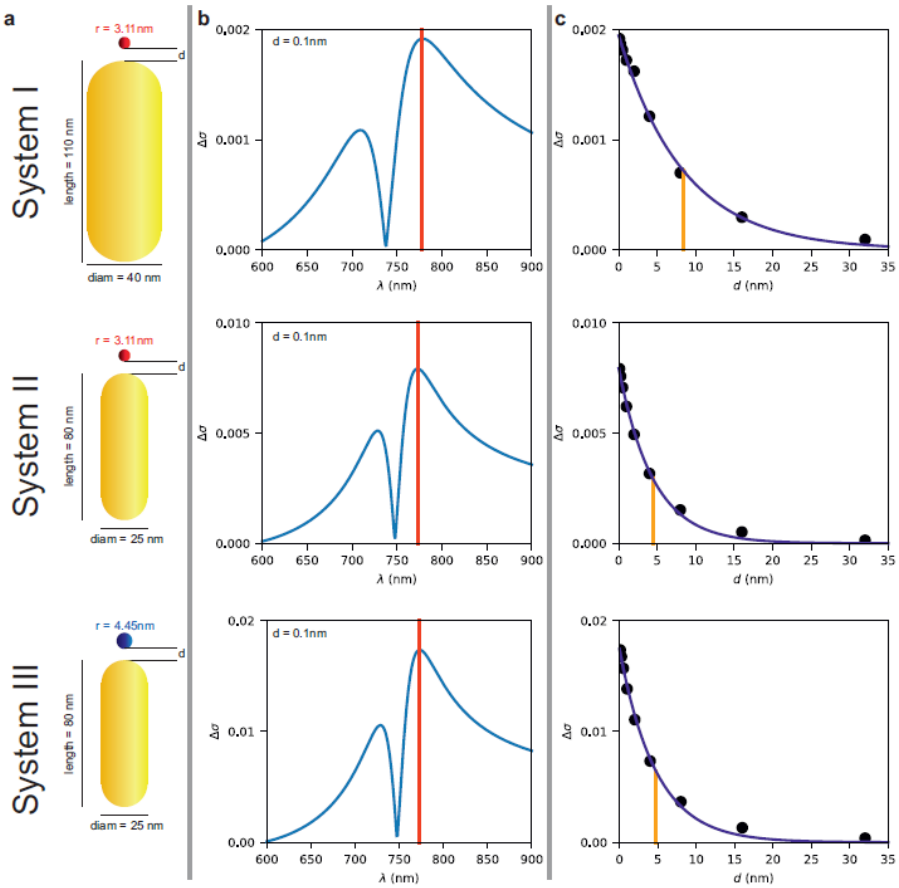

Figure 3.7: Results of BEM simulations. Panels in column **a** show the system dimensions. Red spheres are used for Hem, blue sphere indicates GOx. Panels in column **b** show normalized changes of scattering cross sections $\Delta\sigma$ at a distance d =0.1 nm. The λ_{max} values are indicated as red lines. Panels in column **c** show the distance dependence of $\Delta\sigma$ the orange lines indicate the decay length d_L.

We then fitted exponential decays to these values which allowed us to obtain the

decay length d_L of each system. The relative amplitude values given in the manuscript were computed using system II and III with d =0.1 nm. In order to obtain relative intensity changes for our measurement system we have to take the interference between the reflected and scattered field into account thus we compute $\Delta I_{rel}(\lambda) = (I_k - I_0)/I_0$ with $I_k = R + \sigma_k(\lambda) + 2\sqrt{R\sigma_k(\lambda)}cos(-\pi/2 + \phi(\lambda))$ where $R = \sigma_k(\lambda_{LSPR,k})/R_F^2$ is the reflection coefficient and R_F are the scattered over reflected field ratios determined via polarization scans with parallel polarizer and analyzer performed at the LSPR wavelength. We determine $\phi_k(\lambda) = atan2(Im(L)/Re(L))$ with $L = 1/(i + \frac{\lambda - \lambda_{LSPR,k}}{HWHM})$ by obtaining the half width at half maximum (HWHM) and the resonance wavelength λ_{LSPR} via Lorentzian fits to the $\sigma_k(\lambda)$ values obtained from the simulations. We only do this for systems II and III with the experimentally determined R_F^2 values of 1.7 and 1.8, respectively. The results are displayed in figure. 3.8 and we find that in our interference based system δI_{rel} values of 1.9% (Hem, figure. 3.8a) and 3.5% (Gox, figure. 3.8b) can be achieved. In both cases the maximum δI_{rel} values which can be achieved via interferometric scattering are $\approx$ 2-times higher than the corresponding maximum values achievable via observation of pure scattering.

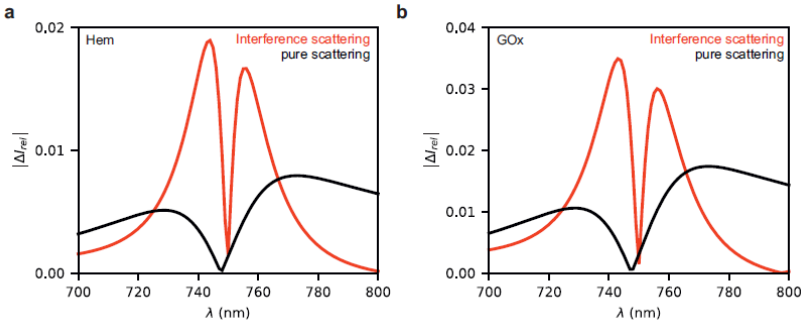

Figure 3.8: Comparison of relative intensity changes. Panels display relative changes of intensity $|\Delta I_{rel}|$ for our interference-scattering based method (red lines) and a pure scattering-based method (black lines). Panel **a** shows results for system II and $R_F^2 = 1.8$. Panel **b** shows results for system III and $R_F^2 = 1.7$.

3.4.4 Statistical Proof of Single-Protein Detection

Here we show that for Hemoglobin, the smallest of our analytes, event rates scale linearly with concentration (figure. 3.9a) and the interevent times follow a Poissonian distribution (figure. 3.9b). This provides statistical evidence for single-protein detection. Further details on this topic can be found in the supplementary material of M.D.

Baaske *at al.* [71].

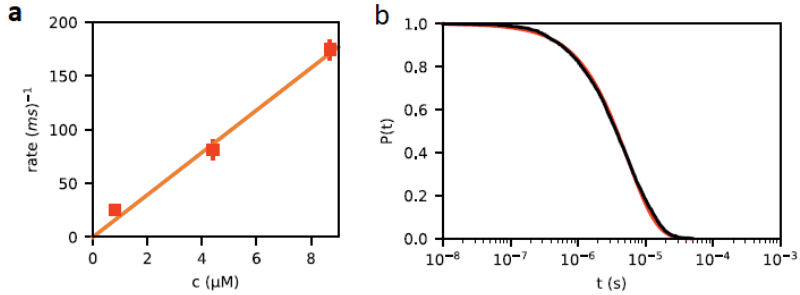

Figure 3.9: Statistical proof for single-protein detection. Panel a shows the dependence of the events rate vs. the concentration of Hemoglobin. We find that the experimental data (squares) follows a linear relationship (linear fit: orange line) as expected for single-protein detection. Panel b shows the probability distribution found for interevent times for Hemoglobin at a concentration of 8.7μM. The black line represents experimental data which shows a good match with respective fit to an exponential decay (red line), *i.e.*, as expected for a Poissonian process. From the fit we determine a rate constant of

3.4.5 Dynamic Light Scattering Measurements

Here we show complementary dynamic light scattering (DLS) measurements performed in order to determine the hydrodynamic radii r_H of our analytes. Both for Hem (figure. 3.10) and GOx (figure. 3.11) we find mono-disperse distributions, which confirm the absence of aggregates. These distributions exhibit center values of $r_H = 3.9\pm1.1$ nm (Hem) and 5.3 ± 1.3 nm (GOx). These values agree well with our experimentally obtained radii of 2.8 ± 0.6 nm (Hem) and 5.8 ± 1.3 nm (GOx) within the errors.

Results

		Size (d.nm):	% Intensity:	St Dev (d.n...
Z-Average (d.nm): 7,703	Peak 1:	7,713	90,0	2,235
PdI: 0,223	Peak 2:	194,0	10,0	78,19
Intercept: 0,892	Peak 3:	0,000	0,0	0,000
Result quality : Good				

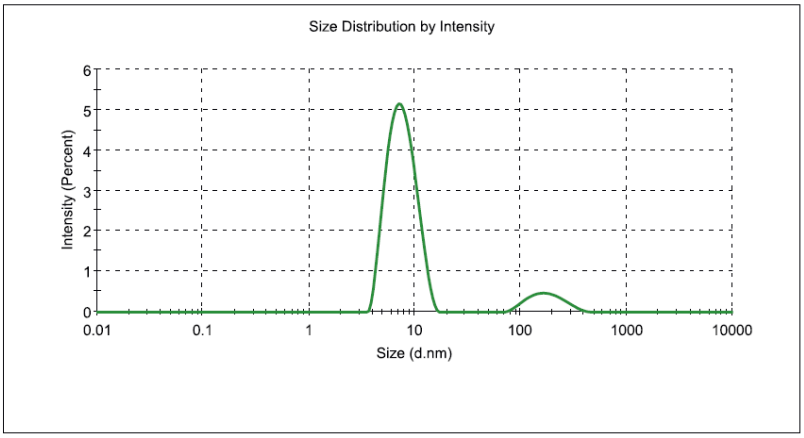

Figure 3.10: Size distribution of Hemoglobin measured via dynamic light scattering Malvern Panalytical Zetasizer). Table values from left to right correspond to peak centers (particle diameter in nanometers), relative intensity attributed to the peak (% Intensity: This is a measure of particle concentration and scattering cross section/size, *i.e.*, the smaller the particles the higher the concentration for a constant percentage of intensity) and the width of the peak (standard deviation) *i.e.* width of the size distribution - the narrower the distribution the more monodisperse is the sample. Peak 1 is caused by the Hemoglobin molecules with a concentration of 50μM in PBS. Peak 2 are contaminants, i.e., bigger particles with in comparison to Hem much lower concentration.

Results

			Size (d.nm):	% Intensity:	St Dev (d.n...
Z-Average (d.nm):	10,16	Peak 1:	10,64	100,0	2,564
PdI:	0,114	Peak 2:	0,000	0,0	0,000
Intercept:	0,767	Peak 3:	0,000	0,0	0,000
Result quality :	Good				

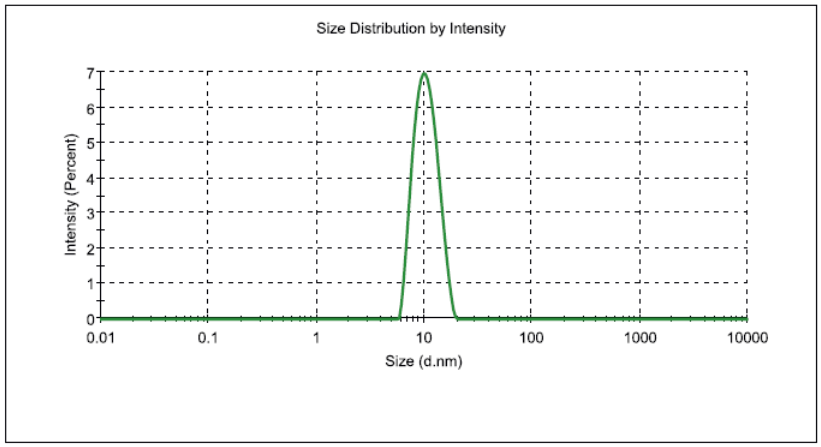

Figure 3.11: Size distribution of Glucose Oxidase measured via dynamic light scattering (Malvern Panalytical Zetasizer). Table values from left to right correspond to peak centers (particle diameter in nanometers), relative intensity attributed to the peak (% Intensity: This is a measure of particle concentration and scattering cross section/size) *i.e.* the smaller the particles the higher the concentration for a constant percentage of intensity) and the width of the peak (standard deviation), *i.e.*, width of the size distribution - the narrower the distribution the more monodisperse is the sample. Peak 1 is caused by the Glucose Oxidase molecules with a concentration of 10μM in a 20 mM NaCl solution.